Generation, transcriptome profiling, and functional validation of cone-rich human retinal organoids

Sangbae Kim[a,1], Albert Lowe[b,c,1], Rachayata Dharmat[a], Seunghoon Lee[d,e,f], Leah A. Owen[g], Jun Wang[a], Akbar Shakoor[g], Yumei Li[a], Denise J. Morgan[g], Andre A. Hejazi[g], Ales Cvekl[b,c], Margaret M. DeAngelis[g,h,i], Z. Jimmy Zhou[d,e,f], Rui Chen[a,2], and Wei Liu[b,c,2]

[a]Human Genome Sequencing Center, Department of Molecular and Human Genetics, Baylor College of Medicine, Houston, TX 77030; [b]Department of Ophthalmology and Visual Sciences, Albert Einstein College of Medicine, Bronx, NY 10461; [c]Department of Genetics, Albert Einstein College of Medicine, Bronx, NY 10461; [d]Department of Ophthalmology and Visual Science, Yale School of Medicine, New Haven, CT 06510; [e]Department of Cellular and Molecular Physiology, Yale School of Medicine, New Haven, CT 06510; [f]Department of Neurobiology, Yale School of Medicine, New Haven, CT 06510; [g]Department of Ophthalmology and Visual Sciences, The University of Utah School of Medicine, Salt Lake City, UT 84132; [h]Department of Pharmacotherapy, College of Pharmacy, The University of Utah, Salt Lake City, UT 84112; and [i]Department of Population Health Sciences, The University of Utah School of Medicine, Salt Lake City, UT 84132

Edited by Jeremy Nathans, Johns Hopkins University, Baltimore, MD, and approved April 11, 2019 (received for review February 1, 2019)

Rod and cone photoreceptors are light-sensing cells in the human retina. Rods are dominant in the peripheral retina, whereas cones are enriched in the macula, which is responsible for central vision and visual acuity. Macular degenerations affect vision the most and are currently incurable. Here we report the generation, transcriptome profiling, and functional validation of cone-rich human retinal organoids differentiated from hESCs using an improved retinal differentiation system. Induced by extracellular matrix, aggregates of hESCs formed single-lumen cysts composed of epithelial cells with anterior neuroectodermal/ectodermal fates, including retinal cell fate. Then, the cysts were *en bloc*-passaged, attached to culture surface, and grew, forming colonies in which retinal progenitor cell patches were found. Following gentle cell detachment, retinal progenitor cells self-assembled into retinal epithelium—retinal organoid—that differentiated into stratified cone-rich retinal tissue in agitated cultures. Electron microscopy revealed differentiating outer segments of photoreceptor cells. Bulk RNA-sequencing profiling of time-course retinal organoids demonstrated that retinal differentiation in vitro recapitulated in vivo retinogenesis in temporal expression of cell differentiation markers and retinal disease genes, as well as in mRNA alternative splicing. Single-cell RNA-sequencing profiling of 8-mo retinal organoids identified cone and rod cell clusters and confirmed the cone enrichment initially revealed by quantitative microscopy. Notably, cones from retinal organoids and human macula had similar single-cell transcriptomes, and so did rods. Cones in retinal organoids exhibited electrophysiological functions. Collectively, we have established cone-rich retinal organoids and a reference of transcriptomes that are valuable resources for retinal studies.

retinal organoid | retinal differentiation | RNA-seq | single cell | cone and rod photoreceptor

Cone and rod photoreceptor cells in the human retina respond to light in visual perception. Although cones are sparse in the peripheral retina, they are enriched in the macula, which is responsible for central vision and visual acuity. Photoreceptor impairment in the macula, in cases such as age-related macular degeneration, has the most impact on vision and is currently incurable. The human macula is challenging to study for the following reasons. The macula is unique to primates; the scarcity and high cost of nonhuman primates limit their use in retinal studies. Mouse models often do not closely recapitulate human macular function and dysfunction, because they lack a cone-rich structure (1).

Stem cell-derived organoids have emerged as powerful models in studying human development and disease (2). Regenerative medicine for the retina is particularly attractive due to its impact on improving the quality of life and the accessibility of the retina (3). A number of research groups, including our own, have generated retinal structures using pluripotent stem cells (4–12) and demonstrated substantially mature cone and rod photoreceptors in long-term retinal organoids (7, 8, 11, 13–17). Specifically, Zhong et al. (8) generated rod-dominant retinal organoids confirmed by their recent follow-up study (14). Li et al. (13) reported seven rod-rich and six cone-rich retinal organoids out of 14 retinal organoids without quantification. Despite these advances, cone-rich retinal organoids resembling the human macula/fovea have not been adequately demonstrated and characterized.

To establish retinal organoids as viable models for retinal studies, rigorous transcriptome profiling and comparison with human fetal and adult retina are essential. Kaewkhaw et al. (12) performed bulk RNA-sequencing (RNA-seq) profiling of sorted CRX+ cells after up to 3 mo of differentiation and identified a group of differentially expressed genes (DEGs) during photoreceptor cell differentiation; the expression of mature photoreceptor markers OPN1MW, OPN1LW, and RHO, however, was barely detectable. Phillips

Significance

Rods and cones are photoreceptor cells with different distributions and functions in the human retina. Rods are dominant at the periphery, which is responsible for peripheral vision; cones are enriched in the macula, which is responsible for central vision and visual acuity. Macular degenerations affect vision the most and are currently incurable. Unique to primates, the macula is challenging to study. Retinal organoids are promising tools in retinal studies, but cone-rich retinal organoids have not been adequately demonstrated and rigorous transcriptome profiling of retinal organoids has not been sufficiently addressed. Here we report the generation, transcriptome profiling, and functional validation of cone-rich human retinal organoids, which resemble the macula/fovea based on the ratio of cones to rods and single-cell transcriptomes.

Author contributions: Z.J.Z., R.C., and W.L. designed research; S.K., A.L., R.D., S.L., L.A.O., J.W., A.S., Y.L., D.J.M., A.A.H., M.M.D., Z.J.Z., R.C., and W.L. performed research; S.K., A.L., R.D., S.L., M.M.D., Z.J.Z., R.C., and W.L. analyzed data; and S.K., Z.J.Z., R.C., and W.L. wrote the paper with contributions from A.L., A.C., and M.M.D.

The authors declare no conflict of interest.

This article is a PNAS Direct Submission.

Data deposition: RNA-sequencing data have been deposited in Gene Expression Omnibus (GEO) database, https://www.ncbi.nlm.nih.gov/geo [accession nos. GSE119274 (RNA-sequencing data) and GSE119343 (single-cell RNA-sequencing data)].

[1]S.K. and A.L. contributed equally to this work.

[2]To whom correspondence may be addressed. Email: ruichen@bcm.edu or wei.liu@einstein.yu.edu.

This article contains supporting information online at www.pnas.org/lookup/suppl/doi:10.1073/pnas.1901572116/-/DCSupplemental.

Published online May 9, 2019.

et al. (18) performed single-cell RNA-seq (scRNA-seq) profiling of long-term retinal organoids and captured photoreceptor gene associations but were unable to reveal individual cell clusters using unbiased algorithms. Collin et al.'s (19) scRNA-seq study of retinal organoids identified cell clusters, but numerous top DEGs were unexpectedly shared by the assigned cone and rod clusters. In contrast, scRNA-seq profiling of the mouse adult retina clearly identified all retinal cell types (20). Retinal cells are classified by a transcriptional code (20, 21). As references, several RNA-seq datasets of human fetal and adult retinas have recently been described (22–27). In addition, Peng et al. (28) recently reported a molecular atlas of macaque foveal and peripheral retinal cells using scRNA-seq. Thus, it is imperative to assess human retinal organoids using comprehensive transcriptome profiling with human and primate retina as references.

In this study, we report the generation, transcriptome profiling, and functional validation of cone-rich human retinal organoids that are reminiscent of the human macula/fovea based on the ratio of cones to rods and single-cell transcriptomes. In addition, cones in retinal organoids display electrophysiological functions. Our experimental system and associated datasets of bulk and scRNA-seq are expected to have broad applications in studying biology of the human retina.

Results

Generation of Cone-Rich Retinal Organoids with Elongated Inner/Outer Segments in Cone Photoreceptors. We sought to generate retinal organoids that are suitable for modeling human retinal development and degenerative disease. Here, we generated cone-rich laminar retinal organoids from H1 hESCs using an improved retinal differentiation protocol (Fig. 1*A*; $n > 3$ experiments) (7). Two lines of human iPSCs reproduced these results. As described previously, single-lumen cysts composed of epithelial cells were efficiently induced by extracellular matrix via embedding hESC aggregates in cold Matrigel followed by growth in an N2B27 medium. Cells in the cysts acquired anterior neuroectodermal/ectodermal cell fates, including primitive retinal progenitors in the eye field (7). Then, the cysts were *en bloc*-passaged. Starting at day 7, the cysts gradually attached to the culture surface and formed adherent colonies. Retinal cells in the adherent colonies efficiently differentiated and regionalized, generating retinal progenitor zones expressing VSX2 (7, 29) and PAX6 (7, 29) on day 15 (Fig. 1*B*; $n = 6/6$ wells of cultures). To generate 3D retinal organoids from the adherent retinal cultures, cell-substrate adhesions at the edges of the adherent colonies were partially interrupted via a short treatment with dispase in our improved protocol. The brief dispase treatment followed by growth in a B27 medium was sufficient to detach the adherent cultures within hours. Retinal progenitor cell patches in the detached cell aggregates spontaneously assembled into a retinal epithelium, retinal organoid, which displayed as a round sphere with a bright ring under an inverted microscope. One week later, FCS (8%) was added to the B27 medium. In our improved protocol, floating retinal organoids were cultured in 24-well plates on an orbital shaker.

Retinal organoids expressed the key markers for retinal differentiation. At day 32, retinal organoids displayed as an epithelial structure expressing retinal progenitor markers PAX6, VSX2, SIX3, and RAX (Fig. 1 *C–F*; $n = 6/6$ retinal organoids). In addition, a small number of POU4F2- and OTX2-positive cells were found in retinal organoids (Fig. 1 *G* and *H*), indicating early differentiation of retinal ganglion cells (RGCs) and photoreceptors, respectively (30, 31). At day 105, retinal organoids expressed VSX2, PAX6, OTX2, and photoreceptor marker RCVRN in a laminar manner (Fig. 1 *I* and *J*; $n = 3/4$ retinal organoids), indicating that retinal differentiation in retinal organoids mimicked embryonic retinogenesis. At the stages from 6.5 mo to 11 mo, retinal organoids highly expressed cone photoreceptor marker OPN1MW/LW and rod photoreceptor marker RHO in protruding hair-like structures (Fig. 1 *K–N*; Movie S1; $n = 6/6$ retinal organoids), indicating differentiating inner/outer segments of cone and rod photoreceptors. Notably, the inner/outer segments of cone photoreceptors were elongated (Fig. 1 *K* and *L*), similar to the morphology of cone photoreceptors found in the human fovea (32). In addition, cone photoreceptors (OPN1MW/LW-positive) were more abundant than rod photoreceptors (RHO-positive) with the ratio of cones to rods as high as 2.8:1 (Fig. 1*O*), reminiscent of the ratio of cones to rods in the human macula/fovea (32, 33). Connecting cilia and maturing disk membrane in photoreceptors were demonstrated by electron microscopy (Fig. 1 *P* and *Q*). Thus, we have generated cone-rich laminar retinal organoids with maturing outer segments of photoreceptors.

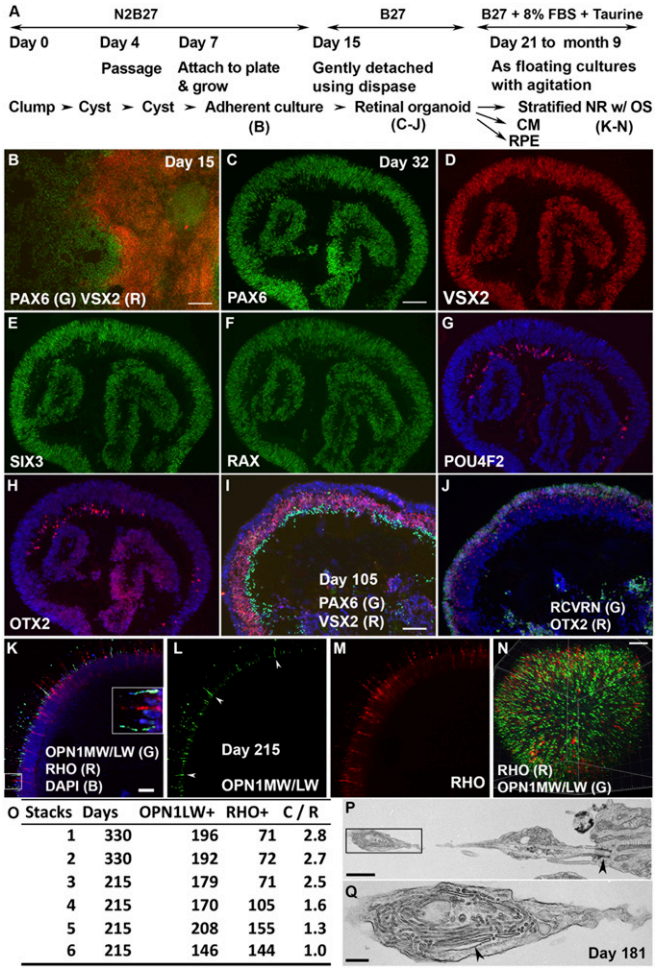

Fig. 1. Generation of cone-rich retinal organoids with elongated inner/outer segments in cone photoreceptors. $n > 3$ experiments. (*A*) A scheme for the generation of cone-rich retinal organoids. (*B*) Adherent cultures on day 15 highly expressed retinal progenitor markers VSX2 and PAX6 ($n = 6/6$ wells of cultures). (*C–H*) Retinal organoids on day 32 continuously expressed retinal progenitor markers PAX6, VSX2, SIX3, and RAX and started to express RGC marker POU4F2 and photoreceptor, bipolar, and horizontal cell marker OTX2 (31) ($n = 6/6$ retinal organoids). (*I* and *J*) Retinal organoids on day 105 expressed VSX2, PAX6, RCVRN, and OTX2 in a laminar manner ($n = 3/4$ retinal organoids). (*K–N*) Retinal organoids on day 215 expressed cone photoreceptor marker OPN1MW/OPN1LW and rod photoreceptor RHO in the protruding hair-like structures ($n = 6/6$ retinal organoids). (*O*) OPN1MW/LW-positive cone photoreceptors were more abundant than RHO-positive rod photoreceptors. Represents six stacks of optical sections in four retinal organoids. One representative optical section in the stacks is shown (*K–M*). C/R, the ratio of cones to rods. (*P* and *Q*) EM of photoreceptors in 181-d retinal organoids. Basal body and maturing disk membrane are shown (arrowheads in *P* and *Q*, respectively). [Scale bars, 200 μm (*B*), 100 μm (*C* and *I*), 50 μm (*K*), 70 μm (*N*), 1 μm (*P*), 0.2 μm (*Q*).]

Transcriptome Profiling of Retinal Organoids in Time Course Using Bulk RNA-Seq. To characterize the transcriptomes during human retinal differentiation, we performed bulk RNA-seq of retinal organoids (34) at multiple time points (15 d and 1, 3, 6.5, and 9 mo; three replicates per time point; *SI Appendix*, Table S1), starting from the stage preceding RGC differentiation to the stage when photoreceptors display outer segments. On average, 33.3 million reads were generated for each sample, with 91.2% of the reads mapped to the reference genome. The RNA-seq dataset had high-quality metrics, including sequencing quality, alignment quality, number of unique mapped reads, and correlation coefficients within replicates (*SI Appendix*, Tables S2 and S3). To assess the reproducibility of biological replicates and the overall patterns across the samples, principal components analysis (PCA) and hierarchical clustering analysis were performed (Fig. 2). In both analyses, retinal organoids at the same time point were grouped together, indicating high reproducibility of biological replicates (Fig. 2*A*) (*SI Appendix*, Table S3). In addition, retinal organoids at 6.5 mo and 9 mo were clustered closely (Fig. 2*A*), indicating their similarity. Further quality assessment of the RNA-seq came from the sequence coverage for transcripts. Overall uniform coverage of transcripts was achieved, which was indicated by 5′- and 3′-bias assessments, including 3′- and 5′- bias calculation, and by manual inspection of retinal marker genes (*SI Appendix*, Fig. S1).

To correlate the transcriptomes generated in this study with the transcriptomes of human retinas and organoids described in previous studies, we compared our dataset with several related datasets (three human adult retinas, eight human fetal retinas at 10 to 23 wk of age, and nine retinal organoids at 0 to 3 mo of age) using PCA and hierarchical clustering (Fig. 2 *C* and *D* and *SI Appendix*, Fig. S2 and Table S4) (12, 22, 25). As shown in Fig. 2*C*, human adult retinas, fetal retinas, and retinal organoids formed three groups. Interestingly, the overall gene expression profiles of retinal organoids were ordered based on their developmental ages (Fig. 2); retinal organoids at 1 mo were similar to human FW10 retina (*SI Appendix*, Fig. S2), and retinal organoids at 6.5 and 9 mo were increasingly similar to human adult retinas (Fig. 2*C* and *SI Appendix*, Fig. S2). Collectively, these unbiased comparative molecular studies indicate that our retinal organoids share numerous molecular features with the human retina.

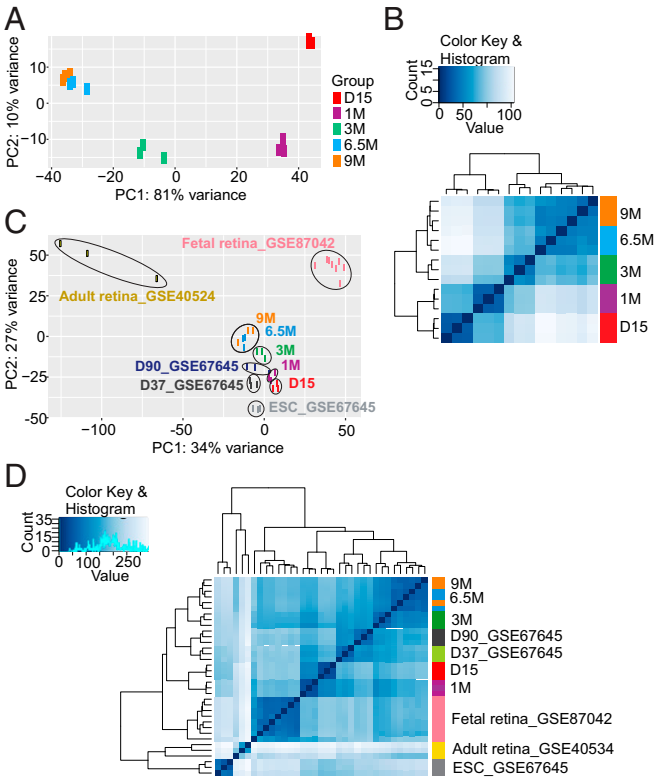

Fig. 2. Visualization of organoid samples based on global expression profiles from RNA-seq data. (*A*) PCA of RNA-seq data from organoid samples. (*B*) Hierarchical clustering analyses were performed using DESeq2 rlog-normalized RNA-seq data. Color code (from white to dark blue) refers to the distance metric used for clustering (dark blue corresponds to the maximum of correlation values). The dendrograms on the left and top of the heat map show the hierarchical clustering of the transcripts for samples. (*C*) PCA of RNA-seq data from organoid samples and published RNA-seq datasets from organoid (GSE67645), human fetal retina (GSE87042), embryonic stem cells (GSE67645), and human adult retina tissues (GSE40524). (*D*) Hierarchical clustering analyses were performed using DESeq2 rlog-normalized RNA-seq data. Color code (from white to dark blue) refers to the distance metric used for clustering (dark blue corresponds to the maximum of correlation values). The dendrograms on the left and top of the heat map show the hierarchical clustering of the transcripts for samples.

Temporal Regulation of the Transcriptomes in Retinal Organoids Follows the Pattern in Retinal Cell Differentiation in Vivo. To investigate the temporal regulation of transcriptomes in retinal organoids as suggested by the clustering dendrograms (Fig. 2*B*), we performed time-course analysis using BRB-Array Tools [false discovery rate (FDR) < 0.05] (35), leading to the identification of 2,334 DEGs that were grouped into four clusters (Fig. 3*A* and Dataset S1). Gene Ontology (GO) analysis of the genes in each cluster using DAVID (36) identified enriched GO terms. Genes in cluster 1 (highly expressed in samples at day 15 and 1 mo) are involved in early development, as GO terms such as "embryonic morphogenesis," "regulation of cell proliferation," "sensory organ development," "BMP signaling pathway," "cell proliferation," and "positive regulation of developmental process" were significantly enriched ($P < 0.00003$) (Dataset S2). Genes in cluster 2 (highly expressed in 1- and 3-mo samples) regulate the differentiation of various retinal cell types, as GO terms such as "neuron differentiation," "sensory organ development," "eye development," "neuron development," and "lens development in camera-type eye" were significantly enriched ($P < 5.8\text{-}E07$). Genes in cluster 3 (high expression at 3-mo samples) regulate neuronal differentiation, as GO terms such as "ion transport," "metal ion transport," "potassium ion transport," "glutamate signaling pathway," "synaptic transmission," and "neuron differentiation" were significantly enriched ($P < 5.8\text{-}E07$). Genes in cluster 4 (highly expressed in the samples at 6 and 9 mo) regulate the maturation of photoreceptor cells, as GO terms such as "visual perception," "detection of light stimulus," "phototransduction," "neurological system process," "photoreceptor cell development," "photoreceptor cell differentiation," and "eye photoreceptor cell development" were significantly enriched ($P < 5.8\text{-}E07$). Time-course analysis of RNA-seq data confirms immunohistochemistry results and indicates that temporal regulation of the transcriptomes in retinal organoids follows the pattern found in retinal development in vivo.

Temporal Expression of Cell Differentiation Markers and Retinal Disease Genes in Retinal Organoids Follows the Conserved Order of Retinal Cell Differentiation in Vivo. To analyze the differentiation of each retinal cell type, we examined the expression of cell lineage-specific markers in the dataset of bulk RNA-seq (Fig. 3*B* and Dataset S3). Retinal neurons and glia are generated from retinal progenitors in an evolutionarily conserved order (37), and the identities of retinal cells are readily identified using a group of cell-specific markers (see Dataset S3 for details) (12, 20, 21). Consistent with our immunostaining showing abundant retinal progenitors at day 15 (Fig. 1*B*), retinal progenitor markers *SIX6*, *FGF19* (known as *Fgf15* in mice), *LHX2*, *LIN28B*, and *PRTG* were highly expressed whereas RGC markers POU4F2 and POU4F1 were not found in RNA-seq samples at day15 (Fig. 3*B*). Between 1 and 3 mo, we observed concomitant down-regulation

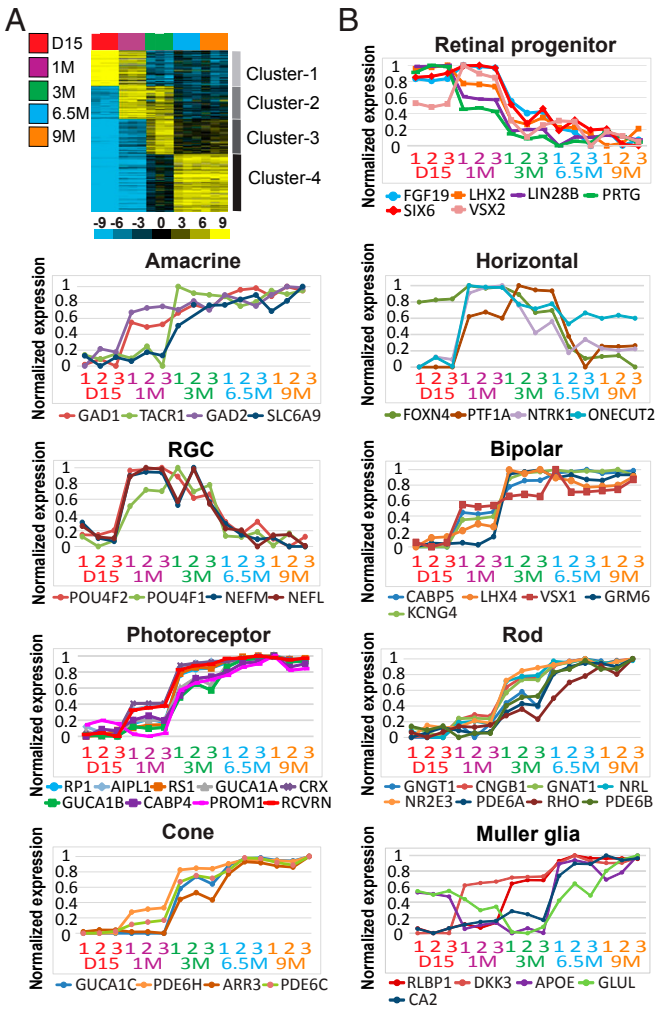

Fig. 3. Temporal regulation of the transcriptomes and cell differentiation markers in retinal organoids. (*A*) After time-course analysis of the RNA-seq data using BRB-Array Tools, four distinct subclusters with 2,334 genes (FDR < 0.05) were identified using k-means clustering. GO term analysis for each cluster is shown in Dataset S1. The rlog-normalized RNA-seq data were centralized by subtracting median expression level across samples, and hierarchical clustering was performed. Each row and column represents gene and sample, respectively. Color scale is indicated at the bottom. (*B*) Dynamic expression of retinal cell specific marker genes during organoid development. The RNA-seq data with log2-transformed read count values were normalized ranging from 0 to 1 across samples and plotted. The *x* axis represents samples ordered by time; the *y* axis represents normalized expression.

of retinal progenitor markers and up-regulation of neuronal markers. For example, RGC markers *POU4F1*, *POU4F2*, *NEFM*, and *NEFL* were strongly up-regulated at 1 mo, consistent with the fact that RGCs are the first-born retinal neurons during retinal development in vivo. The decline in expression of RGC markers at 6.5 and 9 mo confirmed the gradual death of RGCs in retinal organoids due to limitations of the culture system (7). A similar expression pattern was observed for horizontal cell markers *FOXN4*, *PTF1A*, *NTRK1*, and *ONECUT2.* Amacrine cell markers *GAD1*, *GAD2*, *TACR1*, and *SLC6A9* were moderately up-regulated at 1 mo and continued to increase at 3 mo, consistent with the notion that amacrine cells differentiate later than RGCs. Bipolar cell markers (*VSX1*, *CABP5*, *KCNG4*, *GRM6*, and *LHX4*), Müller glial (MG) cell markers (*RLBP1*, *DKK3*, *APOE*, *GLUL*, and *CA2*), rod photoreceptor markers (*GNGT1*, *CNGB1*, *GNAT1*, *NRL*, *NR2E3*, *PDE6A*, *RHO*, and *PDE6B*), and cone photoreceptor markers (*ARR3*, *GUCA1C*, *PDE6C*, and *PDE6H*) were up-regulated starting at 3 mo and remained highly expressed through 9 mo. A large set of transcription factors, including *OTX2*, *THRB*, *CRX*, *NRL*, and *NR2E3*, play critical roles in photoreceptor development and maturation (38). Up-regulation of these genes was initially observed at 3 mo and further increased at 6.5 and 9 mo, consistent with their critical roles in photoreceptor differentiation. Confirming the immunostaining of OPN1MW/LW (Fig. 1 *K*–*N*) and OPN1SW (7), OPN1MW and OPN1LW were absent until 3 mo, but were highly up-regulated at 6.5 and 9 mo. OPN1SW became detectable at 3 mo, and increased at 6.5 and 9 mo, but its expression levels were much lower than those of OPN1MW and OPN1LW (*SI Appendix*, Fig. S3). As retinal differentiation proceeded, proliferation markers MKI67 and MCM2 were down-regulated in retinal organoids in a very similar pattern as seen in human retinal development (*SI Appendix*, Fig. S3). Collectively, temporal expression of cell differentiation markers in retinal organoids is in agreement with the conserved order of retinal cell differentiation in vivo.

To determine the coverage of 266 retinal disease genes documented in RetNet (https://sph.uth.edu/retnet/) in retinal organoids, we examined their expression profiles in the dataset of bulk RNA-seq. As expected, a vast majority of RetNet genes were highly expressed in organoids: On global average, 70% of RetNet genes were ranked within the top 45% of highly expressed genes. In addition, 148 of 266 genes were in the DEG list identified using time-course analysis with BRB-Array Tools (FDR < 0.05) (35) (Dataset S4). About 60% of the RetNet genes were expressed starting at 3 mo and peaked in expression at 6 to 9 mo (*SI Appendix*, Fig. S4). The temporal expression patterns of RetNet genes were consistent with the notion that a vast majority of retinal disease genes are associated with photoreceptor cells. Collectively, the expression of RetNet genes in retinal organoids is developmentally regulated and is consistent with their disease-causing roles in the retina.

Alternative mRNA Splicing in Time-Course Retinal Organoids Follows the Patterns in Human Retinal Differentiation. Alternative mRNA splicing is a major contributor to transcript diversity in human genes, and transcripts often exhibit tissue-specific alternative splicing (39, 40). Indeed, a large number of retina-specific variants have been reported (25, 41). To determine whether the pattern of mRNA splicing in retinal organoids recapitulates that in human retinal tissues, we compared mRNA splicing patterns in organoids with those in human fetal retina, adult retina, and negative control testis tissue. First, a total of 2,969 alternative splicing exons from 2,041 genes that show significant inclusion variance among sample groups were identified. Interestingly, the exon inclusion pattern of organoid samples closely resembled that of fetal retinas, followed by that of adult retinas (Fig. 4*A* and Dataset S5). In addition, the exon inclusion pattern in testis tissues, which served as an outgroup control, was clustered separately from the retinal organoids/tissues. These results suggest that retinal organoids have similar alternative splicing patterns compared with authentic human retinal tissues (Fig. 4*B*). For example, transcript of Receptor Accessory Protein 6 (*REEP6*) gene has two variants, the canonical variant and the retina-specific variant *REEP6.1* (42, 43). As the retina-specific variant is exclusively expressed in rod photoreceptor cells, it is absent or lowly expressed in the fetal retina but highly expressed in the adult retina (see Fig. 6*C*) (43, 44). In retinal organoids, *REEP60.1* was absent at the 15-d and 1-mo time points but gradually increased from 3 mo to 9 mo, coinciding with photoreceptor cell differentiation. As further examples, alternative splicing patterns for retinal genes *GUCA1A*, *GLUL*, and *RXRG* in time-course retinal organoids were similar to those in the human retinas (*SI Appendix*, Fig. S5). Therefore, the mRNA splicing program in retinal organoids reflects that in the human retinal tissues.

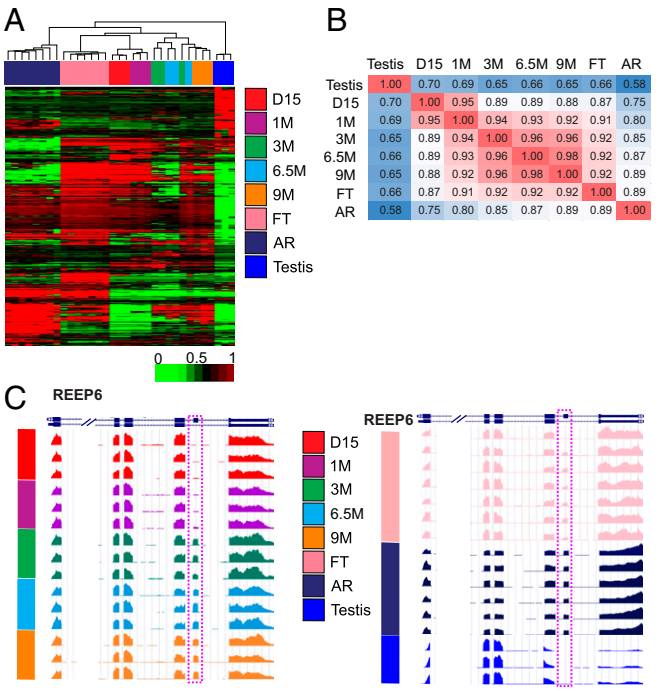

Fig. 4. Comparison of the alternative splicing patterns in organoid, human retina, and testis tissues. (*A*) The heat map shows the comparison of PSI of 2969 alternative SE that show significant (ANOVA test, FDR q-value < 1e-3) inclusion variance in 2,041 genes across different tissues based on RNA-seq data. The hierarchical clustering of exon PSI was performed with Spearman rank correlation. Each row and column indicates exon and sample, respectively. Color scale is shown at the bottom. (*B*) The spearman correlation of PSI of 2,969 SE exons among organoid samples, human fetal retina, and adult retina and testis tissues, were pairwisely estimated. The spearman correlation was computed based on the merged RNA-seq data of the sample groups. (*C*) UCSC Genome Browser view of the exon inclusion pattern of a retinal-specific exon in *REEP6*. Image courtesy of ref. 74. The expression of the *REEP6* exons is shown with sequence coverage depth (quantity of reads, *y* axis) on the gene loci in organoid and human tissues. The RNA-seq data were mapped to Human genome hg19 (GRCh37) using HISAT2 (62, 67). AR, adult retina; FT, fetal retina.

Single-Cell RNA-Seq of 8-mo Organoids Identifies Cell Clusters and Confirms the Cone Enrichment in Retinal Organoids. To gain insight into cell composition and single-cell transcriptomes of retinal organoids, we performed scRNA-seq of 8-mo retinal organoids (45). Transcriptome profiles were generated from a total of 1,130 individual cells from 10 retinal organoids. Four major groups, C0 to C3, were identified, with each accounting for 34%, 25%, 25%, and 15% of the total cells, respectively (Fig. 5*A*). To determine the cell identity of each group, we examined the top 20 genes enriched for each cluster (Fig. 5*B* and *SI Appendix*, Fig. S6). Using the well-established cell-specific markers in the top 20 genes, we assigned cluster_0 (C0) as cone photoreceptor cells, cluster_1 (C1) as rod photoreceptor cells, and cluster_2 (C2) as MG cells, respectively. In contrast, cluster_3 (C3) contained a mixed population of retinal neurons, including bipolar cells, RGCs, and amacrine cells; their relatively low cell fractions in retinal organoids likely prevented discrete cell clustering in scRNA-seq. Therefore, based on scRNA-seq data, 8-mo retinal organoids were mostly composed of photoreceptors, with cone and rod photoreceptors accounting for about 60% of all cells. Strikingly, although the human retina is overall rod-enriched, retinal organoids at 8 mo were rich in cones, with a ratio of cones to rods of 1.4:1, confirming the cone enrichment in retinal organoids initially identified using quantitative multiphoton microscopy.

In addition to identifying individual cell types, the scRNA-seq data allowed us to obtain a single-cell transcriptome for each cell type. Indeed, the top 20 transcripts used for the identification of cone, rod, and MG cells (Fig. 5*B* and Dataset S4) included the vast majority of well-known cell-specific markers (Fig. 3*B* and Dataset S3). Furthermore, a total of 1,110 DEGs were identified using the Wilcoxon rank sum test (adjust *P* value < 0.05 and log fold change > 0.25) in the Seurat package (https://satijalab.org/seurat/). We performed GO analysis of the top 50 genes in each cluster (Dataset S6). Both C0 and C1 were enriched for "visual perception," "sensory perception of light stimulus," and "phototransduction" ($P < 2.01E-10$), whereas C2 was enriched for genes associated with "regulation of cell proliferation" and "response to mechanical stimulus" ($P < 0.0007$) (Dataset S7). GO terms in C3 were enriched for "neuron differentiation" and "cell migration" ($P < 0.0005$). Therefore, single-cell transcriptomes of photoreceptor cells and MG cells in human retinal organoids confirm the well-known cell-specific markers and identify additional cell-specific markers in an unbiased manner.

Comparison of Single-Cell Transcriptomes Demonstrates the Similarity Between Retinal Organoids and Human Macula in Cones and Rods. To determine the similarity between retinal organoids and human

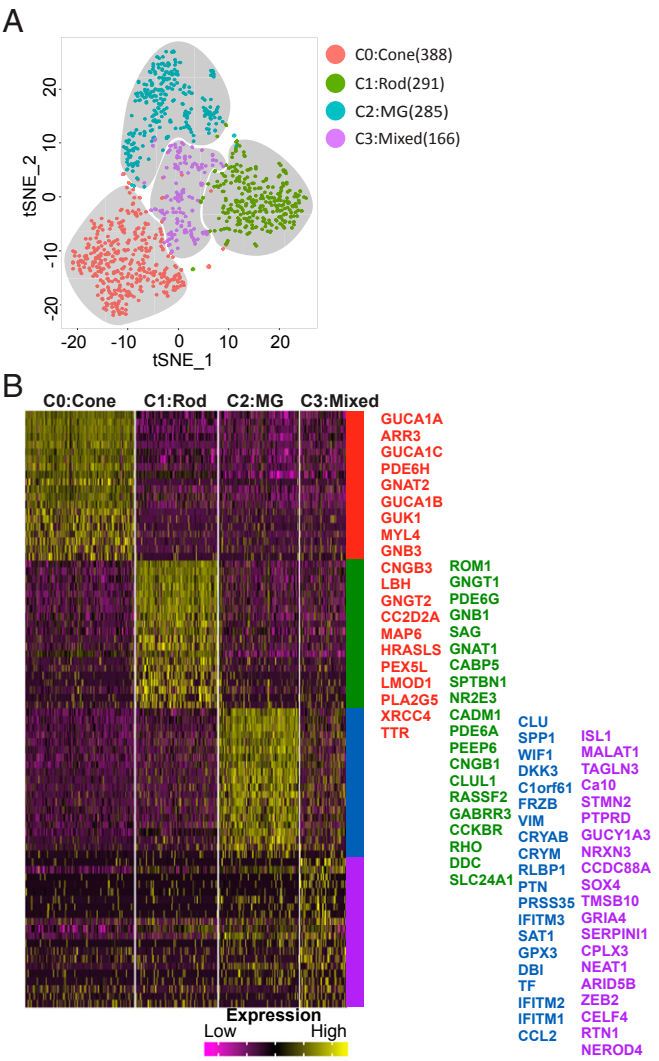

Fig. 5. Identification of cell clusters and confirmation of cone enrichment in 8-mo organoids using t-SNE mappings and nearest-neighbor plots of the scRNA-seq dataset. (*A*) t-SNE plot of single cells in 8-mo organoids based on retinal cell specific markers using the Seurat package (https://satijalab.org/seurat/). (*B*) Heat map of the top 20 genes for each cluster compared with other clusters. Color scale is indicated at the bottom. BP, bipolar cells.

macula, we compared their single-cell transcriptomes. Single-cell transcriptomes of human retina have not been reported. We decided to profile single-cell transcriptomes of well-characterized fresh normal human macula (46, 47) using single-nucleus RNA-seq as a surrogate (referred to as single-cell transcriptomes hereafter for convenience) for these reasons: (*i*) Fresh human retinal tissues are not readily available, (*ii*) cell nuclei are well preserved in frozen human retinal tissues, and (*iii*) single-nucleus RNA-seq is highly correlated to scRNA-seq (48). As described in *Materials and Methods*, single-cell transcriptomes of human macula were successfully generated, resulting in cell clusters of cones, rods, bipolar cells, MG cells, and interneurons (*SI Appendix*, Fig. S7*A*). We compared the single-cell transcriptomes between retinal organoids and adult human macula for each matching cell type. Independent of their source, cells of the same type were clustered together (Fig. 6*A* and *SI Appendix*, Fig. S7*B*), indicating high concordance between retinal organoids and human macula in each matching cell type: cone, rod, and Müller glia. Strikingly, based on 11,051 genes that passed quality control, the correlation coefficient between retinal organoids and human macula was very high for rods (r = 0.98), cones (r = 0.91), and MG cells (r = 0.86) (Fig. 6*B*). Furthermore, expression of the key cell-specific markers for cones, rods, and MG cells was highly concordant between retinal organoids and human macula and was even higher in retinal organoids for multiple markers (Fig. 6*C*). Thus, our retinal organoids and adult human macula are similar in single-cell transcriptomes.

Peng et al. (28) recently reported single-cell transcriptomes of macaque foveal (center of the macula) and peripheral retina using scRNA-seq. Although gene expression that exclusively delineates foveal and peripheral cones or rods was not found, differential gene expression in matched foveal and peripheral cells was identified. For example, the number of DEGs between macaque foveal and peripheral cones is 48, whereas the number of DEGs between foveal and peripheral rods is 15 (diff [log-fold change] > 0.5 or < to −0.5, P adjusted < 1E-05), indicating that the difference between foveal and peripheral cones is more significant than the difference between foveal and peripheral rods is (28). To determine whether our retinal organoids are closer to macaque fovea than macaque peripheral retina, we compared their single-cell transcriptomes. We found that organoid and macaque foveal cones had a higher correlation coefficient (r = 0.98) than organoid and macaque peripheral cones had (r = 0.92) based on the matched 8,393 genes between human and macaque (*SI Appendix*, Fig. S8), further indicating that our retinal organoids are more similar to the fovea than the peripheral retina.

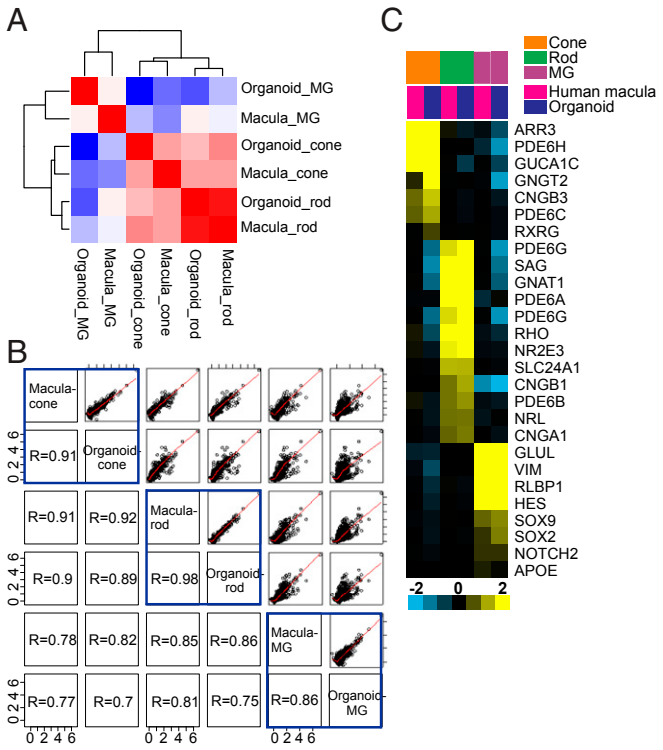

Fig. 6. Comparisons of single-cell transcriptomes between human retinal organoid and macular cone, rod, and MG cells. (*A*) Heat map of correlation matrix of six subgroups: Macula_cone, Organoid_cone, Macula_rod, Organoid_rod, Macula_MG, and Organoid_MG. We merged scRNA-seq data from retinal organoids (1,096 cells) and the human retina (1,322 cells) and assigned the retinal cell type on subclusters in the t-SNE plot using the Seurat package (https://satijalab.org/seurat/). Next, we selected cone, rod, and MG cell clusters of organoid and human macula and then generated average profile of each group across genes. Then, a correlation matrix was calculated and visualized using R. (*B*) Pairwise scatter plot of six subgroups. The upper shows scatter plot and lower shows correlation coefficient values between pairs. (*C*) Expression of marker genes for cones, rods, and MG cells in six subgroups. Color scale for centered gene expression is indicated in the bottom. BP, bipolar cells.

Functional Test of Cones in Retinal Organoids. To assess the functional status of cone photoreceptors in the organoid, whole-cell patch-clamp recording was made from individual cones in a flat-mount preparation. Cones were targeted for recording based on their larger soma size compared with that of rods in the outer nuclear layer (Fig. 7*A*). The morphology of cones was verified by 3D reconstruction under a two-photon microscope (Fig. 7*B*). When recorded under voltage clamp in a K^+-based intracellular solution (*Materials and Methods*), cones in 5- to 8-mo organoids displayed a variety of voltage-gated currents. In particular, we found that all recorded cones (n = 18) exhibited an inward current, which was activated by hyperpolarizing voltage steps from a holding potential of −50 mV (Fig. 7*C*), suggesting the expression of functional HCN channels. Application of CsCl (1 mM) reversibly blocked this current (n = 3, Fig. 7*C*), consistent with the well-known pharmacology of HCN channels. The mean whole-cell conductance of HCN channels was 5.4 ± 0.5 nS (n = 8) between −60 and −120 mV (Fig. 7*D*). The current activation kinetics could be fit with a single exponential function. The activation time constant (tau) was membrane potential-dependent (Fig. 7*E*) and had a value of 65 ± 6 ms (n = 8) at −80 mV, consistent with the activation kinetics of HCN currents reported for cones in the vertebrate retina (49–51). Notably, this activation time constant is similar to that of the homogenously expressed HCN1 (~80 ms, at ~ −90 mV), but much smaller than those of HCN2, HCN3, and HCN4 (~500 ms, ~1,500 ms, and ~3,500 ms, respectively) (52–54), suggesting that cones in our organoids expressed predominantly HCN1. Indeed, scRNA-seq of 8-mo organoids detected HCN1 transcripts along with other photoreceptor-specific transcripts (e.g., GUCA1C and recoverin) in the cone cluster (Figs. 3*B* and 7*F*). HCN1 transcripts were also detected from bulk RNA-seq of retinal organoids at various ages. The developmental profile of the bulk HCN1 transcripts revealed a large rise in HCN1 transcripts beginning at ~3 mo, similar to (or slightly ahead of) the developmental expression profile of OPN1MW (Fig. 7*G*). By comparison, the transcripts of other three HCN isoforms (HCN2, HCN3, and HCN4) were at much lower levels throughout organoid development (Fig. 7*G*). Thus, hESC-derived cones in our organoids expressed functional HCN1 channels, consistent with a characteristic physiological feature of human and other vertebrate cone photoreceptors (49–51, 55).

Discussion

Here we report the generation and characterization of cone-rich functional retinal organoids that are differentiated from human pluripotent stem cells. The cone enrichment was initially identified by quantitative analysis of OPN1MW/LW+ and RHO+ cells using multiphoton microscopy and subsequently confirmed

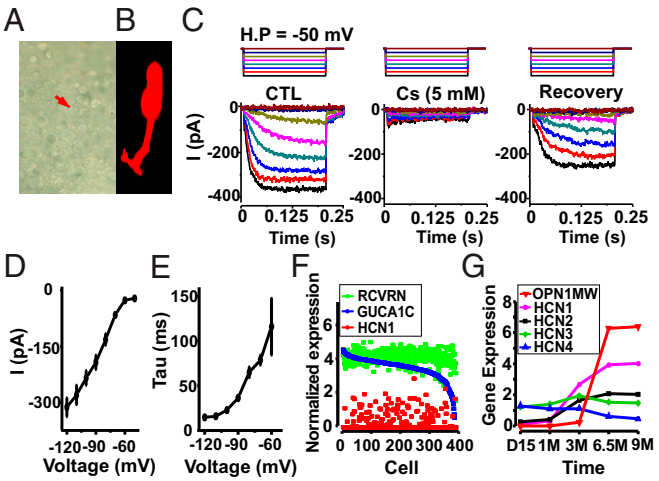

Fig. 7. Expression and functional characterization of HCN channels of cone photoreceptors in cultured organoids. (*A*) Photomicrograph of a 200-d organoid in flat mount, showing the outer nuclear layer. (*B*) Cross-sectional view of a dye-filled cone (marked by arrow in *A*), reconstructed from a z-stack of two-photon images taken after patch clamp, showing the inner segment, soma, axon, and axon terminals of the cell (the outer segment was missing after removal of patch pipette). (*C*) Whole-cell voltage-clamp recording from a cone, showing leak-subtracted HCN currents (bottom traces) in response to seven hyperpolarizing voltage steps (in 10-mV amplitude increments, top traces) from a holding potential of −50 mV (*Left*) and reversible blocked by 5 mM CsCl (*Center* and *Right*). (*D*) Current-voltage relation (measured at plateau amplitudes) of HCN currents in eight cones. (*E*) Activation time constant of HCN current as a function of test voltage (holding potential: −50 mV, $n = 8$). (*F*) Normalized expression [ln(read count + 1)] of HCN1, GUCA1C, and recoverin in the cone cluster in scRNA-seq of 8-mo organoids. (*G*) Expression profiles [log2(RFKM + 1)] of HCN1, HCN2, HCN3, HCN4, and OPN1MW in bulk RNA-seq of organoids.

using scRNA-seq. The retinal organoids were reminiscent of the human macula/fovea based on the ratio of cones to rods and the single-cell transcriptomes. The cones in retinal organoids had functional HCN channels with kinetic properties consistent with the predominant expression of HCN1 transcript in the cone cluster, indicating their electrophysiological functionality. The cone-rich retinal organoids and associated datasets of transcriptomes revealed by bulk RNA-seq and scRNA-seq are useful resources in studying human retinal cell differentiation and inherited retinal disease.

Our cone-rich human retinal organoids mimic the macula/fovea in multiple aspects. First, both retinal organoids and the macula/fovea are rich in cones. Based on immunostaining of OPN1MW/LW and RHO, the ratio of cones to rods in retinal organoids was in the range of 1:1 to 2.8:1. Based on the cell clusters identified using the top 50 DEGs in scRNA-seq, the ratio of cones to rods was 1.4:1, representing the average in 10 retinal organoids. In the human retina, the ratio of cones to rods is 1:20 in the peripheral regions and 1:8 in the macular region; in the fovea, the center of the macula, photoreceptors are mostly composed of cones (33, 56). Therefore, the ratio of cones to rods in our retinal organoids is higher than the ratio found in the macula and lower than the ratio in the fovea. The regulator for cone commitment is still elusive (57), although thyroid hormone signaling directs cone subtypes in mice and human retina (16, 58). In our floating culture, abundant cone photoreceptors spontaneously differentiate from $VSX2^+$ epithelium, consistent with the default cone commitment hypothesis in the retina (57). The long-term culture medium in our previous (7) and current studies did not contain any exogenous retinoic acid, which promotes rod development (59), likely contributing to a permissive condition for cone differentiation. Related to this concept, Zhong et al. (8) supplemented retinoic acid in their culture medium and generated retinal organoids that had "rod-dominant ONL." In their recent follow-up paper, Capowski et al. (14) confirmed that their retinal organoids were rod-dominant. These findings indicate that retinoic acid may oppose cone differentiation in retinal organoids. Alternative to the default cone commitment hypothesis, unknown instructive factors may direct cone cell differentiation in the retina in vitro and in vivo (57).

Second, comparisons of single-cell transcriptomes demonstrated the similarity between retinal organoids and human macula in cones and rods. Since RGCs degenerated in retinal organoids due to limitations of the culture system, the cell composition in long-term retinal organoids and the macula differs. Bulk RNA-seq does not distinguish the global difference in transcriptomes caused either by varied expression levels in individual cells or by varied cell composition in tissues. In contrast, scRNA-seq measured the transcriptomes in each cell type and removed the noise caused by varied cell composition, making it more accurate. It would be ideal to assess the similarity between retinal organoids and the macula using macula-specific markers, but such markers remain elusive despite several transcriptomic comparisons (23, 27, 28, 56). Nevertheless, high concordance in the single-cell transcriptomes between retinal organoids and human macula in cones and rods indicated their similarity. In addition, organoid and macaque foveal cones had a higher correlation coefficient than organoid and macaque peripheral cones had, further indicating that our retinal organoids are more similar to the fovea than the peripheral retina.

We present evidence that our retinal organoids are similar to the human macula in multiple aspects, but we do not intend to claim that they are equivalent. Indeed, photoreceptor outer segments in retinal organoids have not reached mature state yet. The disk membrane in photoreceptors reported here and in our previous study (7) was oblique, resembling the disk membrane in mouse photoreceptors at postnatal days 6 to 10 (60). Engineering retinal pigment epithelium (RPE) in close contact with photoreceptor outer segments may facilitate further differentiation of disk membrane in photoreceptors.

Our bulk RNA-seq outlines a molecular roadmap from human retinal progenitors to retinal neurons and our scRNA-seq provides insight into the transcriptomes of human photoreceptors at a single-cell level. Instead of using sorted CRX+ cells up to early stages of photoreceptor differentiation (12), our bulk RNA-seq used whole retinal organoids covering the stages when photoreceptors are substantially mature, providing insight into human retinal differentiation for all retinal cell types over a wide timespan. The present bulk RNA-seq studies of retinal organoids confirmed that the differentiation of retinal neurons in vitro follows the evolutionarily conserved order of retinogenesis in vivo (37). In addition, our bulk RNA-seq revealed retina-specific alternative mRNA splicing (*REEP6* as an example), as well as the expression patterns of retinal disease genes. Our scRNA-seq identified cell clusters, confirmed the cone enrichment, identified known and unknown cell-specific markers for photoreceptors, and allowed us to compare single-cell transcriptomes between retinal organoids and the human macula. Our scRNA-seq confirmed and expanded the findings revealed by bulk RNA-seq and immunostaining. Collectively, our bulk RNA-seq and scRNA-seq datasets establish a comprehensive reference of transcriptomes in studying human retinal differentiation.

Although retinal organoids with differentiated cone and rod photoreceptors were previously reported by us and others (7, 8, 11, 13–17), the ratio of cones to rods has not been rigorously determined using scRNA-seq until the current study. Based on immunostaining, Li et al. (13) found seven rod-rich and six cone-rich retinal organoids out of 14 retinal organoids, but the ratio of cones to rods was not quantified. In contrast to our findings, Li et al.'s (13) retinal organoids expressed L/M opsin and rhodopsin in the cytoplasm and did not display overt inner and outer segments of photoreceptors. Eldred et al. (16) determined the ratio of S cones to L/M cones but did not quantify the ratio of cones to rods. Two recent scRNA-seq studies of long-term retinal organoids

did not report the ratio of cones to rods (18, 19). In contrast to the cone (34% of total cells) and rod (25% of total cells) cell clusters in our scRNA-seq study, Phillips et al. (18) did not identify individual cell cluster using unbiased algorithms. Collin et al. (19) identified cone and rod cell clusters in a combined dataset containing retinal organoids at days 60, 90, and 200, but numerous top DEGs were unexpectedly shared by the assigned cone and rod clusters. Indeed, our analysis of Collin et al.'s (19) scRNA-seq dataset for 200-d retinal organoids identified a cell cluster (15.3% of total cells) that contains both rod and cone photoreceptors. Thus, cell compositions and single-cell transcriptomes vary significantly in retinal organoids generated in different laboratories; cone enrichment in our retinal organoids is robustly demonstrated using both quantitative microscopy and scRNA-seq profiling.

In summary, our cone-rich retinal organoids mimic the human macular retina in numerous cellular and molecular aspects. With further improvement of retinal organoids and the power of gene delivery and editing tools, it is conceivable that retinal organoids will play increasing roles in functional studies of genetic variants/mutations and therapeutic development for blinding retinal diseases.

Materials and Methods

Maintenance of hESCs. Embryonic Stem Cell Research Oversight and IRB committees at Albert Einstein College of Medicine approved the project. Undifferentiated H1 hESCs (WiCell WA01) or hiPSCs (Corriell Institute AICS 0023) were grown on Matrigel-coated six-well plates in mTeSR1 medium and passaged using ReLeSR (STEMCELL Technologies) as previously described (7).

Retinal Cell Differentiation. Retinal cell differentiation from H1 hESCs was performed using our previous protocol (7) with modifications. A humidified incubator at 37 °C with 5% CO_2 was used for culture. Briefly, small aggregates of hESCs (or hiPSCs) were suspended in ice-cold Matrigel. After gelling at 37 °C for 20 min, the hESC/Matrigel clump was gently dispersed in an N2B27 medium [DMEM/F12 (Gibco):neurobasal medium (Gibco) = 1:1, 0.5× B27 supplement (Gibco), 0.5× N2 supplement (Gibco), 0.1 mM β-mercaptoethanol, and 2 mM GlutaMAX] for floating culture. With the starting day of cell differentiation designated as day 0, single-lumen cysts formed on day 1. On day 4 or 5, floating cysts were passaged to new 24-well plates at a density of 20 to 40 cysts per well. Starting at day 7, cysts spontaneously attached to the culture surface and grew. On day 15 (days 13 to 17 gave similar results) in our improved protocol, the adherent cultures were partially lifted at their edges via a 3-min dispase treatment (0.5 mg/mL in DMEM/F12), rinsed with DMEM/F12 medium, and then grown in a B27 medium [DMEM/F12 (3:1), 2% B27, and NEAA]. Within hours, the adherent cultures were spontaneously detached to form floating aggregates. In about 1 wk, retinal organoids spontaneously formed, displaying a bright ring when viewed under an inverted microscope, and were grown (three to five retinal organoids per well on 24-well plates) in a serum medium [DMEM/F12 (3:1), 8% FCS (26140095; Gibco), 2% B27, NEAA, 100 mM taurine (Sigma), and 2 mM GlutaMAX] on an orbital shaker in our improved protocol. Medium was changed every 3 d unless stated otherwise.

Immunostaining and Antibodies. Retinal organoids and adherent cultures were fixed in 4% paraformaldehyde for 15 to 30 min at room temperature and processed for immunostaining. Cryosections (8 μm) of retinal organoids were used. The primary antibodies are L/M-opsin (1:2,000; from J. Nathans, Johns Hopkins University, Baltimore), OTX2 (1:1,500; R&D AF1979), PAX6 (1:500; Covance PRB-278P), POU4F2 (Santa Cruz; SC-6026, 1:200), RAX (1:500; Abcam ab86210), RCVN (1:2,000; Millipore AB5585), RHO (ab98887; 1:500; Abcam), SIX3 (1:500; Rockland), and VSX2 (1:500; Millipore AB9016). Primary antibodies were visualized using Alexa Fluor 488- or 568-conjugated secondary antibodies and imaged using a Zeiss AxioObserver Z1 microscope.

Cell Counting. Retinal organoids at 6.5 to 9 mo displayed similar expression profiles based on bulk RNA-seq analysis and immunostaining, and thus were considered as one group. Retinal organoids (two at day 215 and two at day 330) were immunostained in whole mount using antibodies against OPN1MW/LW and RHO. Stacks of images were taken using Olympus FV1000-MPE multiphoton microscope with an objective (25×, N.A. 1.05). Immunostaining in the inner/outer segments at the apical surface of retinal organoids in every eighth optical section in stacks was counted, with four to six optical sections in each stack. In total, six stacks of optical sections in four retinal organoids were counted.

EM. EM of retinal organoids at day 181 was performed as described previously (7).

Bulk RNA-Seq of Retinal Organoids. Retinal organoids/cultures at the following time points were used for RNA isolation using TRIzol (Invitrogen): (*i*) day 15, three wells of adherent cultures on a 24-well plate; (*ii*) day 30, three pools with 15 retinal organoids in each pool; (*iii*) day 85 to 94, one pool on day 85 and two pools on day 94 with three retinal organoids in each pool; (*iv*) days 194 to 195, three pools with three retinal organoids in each pool; (*v*) days 248 to 259, three pools with two retinal organoids in each pool. The samples are summarized in *SI Appendix*, Table S1. Libraries were prepared from ∼500 ng of total RNA with the TruSeq Stranded Total RNA Library Prep Kit according to the manufacturer's directions (Illumina). Paired-end 100-cycle sequencing was performed on HiSeq 2000 or HiSeq 2500 sequencers according to the manufacturer's directions (Illumina).

Preparation of Single-Cell Suspensions of Retinal Organoids. Ten retinal organoids on day 248 were dissociated using papain-based enzymatic digestion as described previously (21) with slight modifications (*SI Appendix*, Table S1). Briefly, 45 U of activated papain solution (LS003126; Worthington) with 1.2 mg L-cysteine (Sigma) and 1,200 U of DNase I (Affymetrix) in 5 mL of HBSS buffer was added to the organoids and incubated at 37 °C for 40 min to release live cells. Postincubation, the single-cell solution was centrifuged at 200 × *g* and the papain was deactivated with ovomucoid solution [15 mg ovomucoid (Worthington Biochemical) and 15 mg BSA (Thermo Fisher Scientific) in 10 mL of MEM (Thermo Fisher Scientific)]. The remaining organoid clumps were further triturated in the ovomucoid solution and filtered through a 20-nm plastic mesh. The collected cells (>90% viability) were stained with Ready probes cell viability imaging kit (blue/red) containing Hoeschst 33342 and propidium iodide (R37610; Thermo Fisher Scientific) and were diluted to 3E4 per mL with 1× PBS (Thermo Fisher Scientific), RNase inhibitor (40 KU/mL; NEB), and Cell Diluent Buffer (640167; Takara Bio).

Preparation of Single-Nucleus Suspensions of Macular Punches in the Human Retina. In collaboration with the Utah Lion's Eye Bank, we obtained adult human donor eyes within 6 h postmortem. Both eyes within a given donor had to be diagnosed as normal (defined as no drusen, no choroidal neovascularization, no fibrosis, and no atrophy) according to the Utah Lion's Eye Bank.

Protocol for postmortem phenotyping of donor eyes (47) for one donor eye to be utilized in the study. Briefly, retinal tissue was then immediately dissected from the RPE and choroid. A 4-mm macular region of retina was punched and flash-frozen at −80 °C. Institutional approval for use of human eyes was obtained from the University of Utah and conformed to the tenets of the Declaration of Helsinki. All retinal tissues were deidentified in accordance with Health Insurance Portability and Accountability Act privacy rules.

Nuclei from frozen retinal tissue were isolated using RNase-free lysis buffer (10 mM Tris·HCl, 10 mM NaCl, 3 mM MgCl2, and 0.1% Nonidet P-40). The frozen tissue was resuspended in ice-cold lysis buffer and triturated to break the tissue structure. The tissue aggregates were then homogenized using a Wheaton Dounce Tissue Grinder and centrifuged (500 × *g*) to pellet the nuclei. The pellet was resuspended in fresh lysis buffer and homogenized to yield a clean single-nuclei suspension that was then counterstained with DAPI (10 μg/mL). A single nuclei suspension was prepared in 1,000 μL of 3E4 per mL in PBS (Thermo Fisher), RNase inhibitor (40 KU/mL; NEB), and Cell Diluent Buffer.

ICELL8-Based Single-Cell Capture, Single-Cell RT-PCR, and Library Preparation. Using ICELL8 multisample nanodispenser (Wafergen Biosystems), 50 nL (3E4 per mL) of the live cell or nuclear suspension was precisely dispensed into an ICELL8 nanowell microchip containing 5,184 wells (150 nL capacity) as described previously (61). Assuming a Poisson distribution frequency for the number of cells per well, about 30% of the nanowells were expected to contain a single nucleus under optimal conditions. Automated scanning fluorescent microscopy (using Olympus BX43 fluorescent microscope with a robotic stage) of the microchip was used to select ∼1,400 wells containing a single live cell or a single nucleus (CellSelect software; Wafergen Biosystems). The candidate wells were manually evaluated for debris or clumps as an additional quality control. The chip was subjected to freeze–thaw to lyse the cells and 50 nL of reverse transcription and amplification solution (following ICELL8 protocol) was dispensed using the multisample nanodispenser to candidate wells. Single-cell RNA barcoding and sequencing was then performed on the candidate wells using preprinted primer that adds a well-specific barcode to the (A)n mRNA tail of the cellular transcript. The cDNA libraries were pooled, concentrated (Zymo Clean and Concentrator Kit; Zymogen) and purified (using 0.6× AMPure XP beads). The 3′ transcriptome enriched library was made by

Nextera XT Kit and 3′-specific P5 primer and sequenced on an Illumina Hiseq 2500. Individual FASTQ files obtained were demultiplexed using the well-specific barcode identifiers for downstream data processing and analysis.

Bulk RNA-Seq Data Processing.

Mapping and data processing. FASTQ sequences of organoid samples were mapped to human genome hg19 (GRCh37) using TopHat2 (62). Aligned reads were counted per gene using HTseq (https://htseq.readthedocs.io, version 0.6.0) using default parameters. Transcript structure and abundance were estimated using Cufflinks (63). The expression of each gene was presented in fragments per kilobase of transcript per million mapped reads (FPKM). The matrix data of read count and FPKM were generated for preprocessing.

PCA and pairwise comparison. For statistical test and data visualization, read count data were transformed with the regularized-logarithm transformation (rlog) function in DESeq2 (version 1.10.1) (64). To determine the similarity across samples, rlog-transformed data were used for PCA using plotPCA of DEseq2 and pairwise comparison of all samples using Pearson's correlation coefficients in R (version 3.5.0). We performed the hierarchical clustering to the heatmap after calculating Euclidian distance with pairwise comparison output in R.

Time-course analysis. To identify genes that were differentially expressed over time, we used the time-course analysis plug-in providing regression analysis of time series data from BRB-Array Tools (version 4.5.1) (35). The 2,334 significant genes for further analysis were selected using an FDR < 0.05. Then, k-means clustering ($k = 4$) with the expression profile of the genes was performed and visualized with a heat map using Gene Cluster 3.0 and Java TreeView (65).

Clustering and visualization. To investigate expression signature, we performed hierarchical clustering and identified the subclusters for major retinal cell classes (RGCs, photoreceptors, bipolar cells, horizontal cells, amacrine cells, MG cells, etc.) using retinal cell marker genes (*SI Appendix*, Table S7). PCA was performed to map high-dimensional data to a 2D space while preserving local distances between samples. The hierarchical clustering of exon inclusion percentage was performed using Gene Cluster 3.0 and was shown using Java TreeView. In GO analysis, the significant enriched processes were identified by P value less than 0.001 using DAVID (https://david.ncifcrf.gov).

Public bulk and scRNA-seq data processing. To compare transcriptome with other datasets, we downloaded published RNA-seq datasets from GEO (https://www.ncbi.nlm.nih.gov/geo): three samples at two time points (days 37 and 90) from human retinal organoid (GSE67645), eight samples (FW-10, 14, 17, 18, 19, 20, 21, and 23) from human fetal retina (GSE87042), three samples (undiff-1, -2, and -3) from embryonic stem cells (GSE67645), and three samples human adult retina tissues (GSE40524). These data were processed in the same way we have done previously for our organoid RNA-seq data. The read count datasets were normalized using DESeq2 and used for PCA and clustering analysis (64).

Alternative splicing pattern analysis. First, the alternative skipped exons (SE) were annotated with hg19 refSeq genes from the UCSC Genome Browser using an open source pipeline, rnaseqlib (https://rnaseqlib.readthedocs.io/en/clip). The RNA-seq data of organoid samples, human fetal retinal cells (GSE67645), adult peripheral retina tissues (GSE94437), and testis tissues (ERP023317) were mapped to human genome hg19 (GRCh37) using TopHat2/HISAT2, respectively (62, 66, 67). To identify differentially spliced variants or exons across samples, we applied a probabilistic framework, MISO (Mixture of Isoforms), to the annotated SE exons with the RNA-seq data (68). Based on the mapped RNA-seq reads, MISO estimated the percent spliced in (PSI) scores of each SE exon in each tissue sample. Then, an ANOVA test was performed to identify the SE exons with significant PSI variance across different sample groups. After multiple testing corrections, we identified 2,969 SE exons in 2,041 genes with FDR q-value $<$ 1e-3. Next, the unsupervised hierarchical clustering was performed to the PSI matrix of the 2,969 SE exons using Gene Cluster 3.0 and visualized with Java TreeView (65). Finally, to compare the overall similarity of splicing pattern among tissues, we calculated the PSI of each exon in each tissue sample group (based on the merged RNA-seq data of samples of the same tissue group) and computed Spearman correlation coefficients among tissues.

scRNA-Seq Data Processing.

Mapping and data processing. For scRNA-seq data analysis, FASTQ files were generated from Illumina base call files using bcl2fastq2 conversion software (v2.17). Sequence reads were aligned to the human genome hg19 (GRCh37) using STAR alignment software (https://github.com/alexdobin/STAR, version 2.5.1b) with default parameters. For transcriptome analysis, aligned reads were counted per gene using HTseq (https://htseq.readthedocs.io, version 0.6.0) using default parameters. Next, we used the Seurat package (https://satijalab.org/seurat/, version 2.3.4) for data analysis including quality control, normalization, dimensional reduction, clustering, and visualization. Cells were filtered based on a minimum number of 600 expressed genes per cell, and all genes that were not detected in at least 5% of all our single cells were discarded for all further analyses.

Normalization and data scaling. After filtering unwanted cells from the dataset, we applied a global-scaling normalization method LogNormalize of Seurat to normalize the data. In this step, gene expression measurements were normalized by total expression, multiplied by a scale factor (10,000 by default), and then log-transformed.

Dimensionality reduction and visualization. Highly variable genes (HVGs) were identified through calculating the variance and mean for each gene in the dataset using FindVariableGenes in the Seurat package with default parameters. Genes were sorted by their variance/mean ratio, and the top 1,000 HVGs were used for PCA. The graph-based method was used to cluster cells. To reduce the high-dimensional gene expression matrix to its most important features, we used PCA to change the dimensionality of the dataset from (cells $\times$ genes) to (cells $\times$ M), where M is a user-selectable number of principal components. After running PCA, PCA-reduced data with 10 PCs were transposed and visualized into 2D space plot using t-SNE, a nonlinear dimensionality reduction method.

Identifying cluster-specific genes. We identified cluster-specific genes by Wilcoxon rank sum test using FindAllMarkers in Seurat with min.pct = 0.25 and other default parameters, selected top 20 genes in a specific cluster compared with others at adjusted P value < 0.05, and visualized the data with a heat map. In addition, we assessed the expression level of retinal specific markers in clusters using a violin plot.

Removing batch effect between organoid and macular scRNA-seq data. For comparing organoid with human macular scRNA-seq data, we used Combat to remove the obvious batch effect with a parametric empirical Bayesian adjustment mode in the sva R package (69, 70). Normalized expression profiles of cone, rod, and MG cells from organoid and macular scRNA-seq data were used for batch effect adjustment. Tissue origin and cell type were used as covariates to create a model. Next, we calculated the average expression value of each gene by each retinal cell type, resulting in the adjusted expression matrix with six columns and 11,051 rows. Then, we computed pairwise Pearson's correlation coefficient among cell types and generated a correlation plot in R. The expression profile was visualized using Gene Cluster 3.0 and Java TreeView.

Statistical Analysis. DEGs over time in bulk RNA-seq profiling were identified using the time course analysis plug-in providing regression analysis of time series data from BRB-Array Tools (version 4.5.1) (35) with an FDR < 0.05. In GO analysis, significant enriched processes were identified using DAVID with P value $<$ 0.001. For alternative splicing analysis, ANOVA test was performed to identify the skipped exons with significant PSI variance across samples, with FDR q-value $<$ 1e-3. The samples for alternative splicing analysis were the RNA-seq data of organoid samples, human fetal retinal cells (GSE67645), adult peripheral retina tissues (GSE94437), and testis tissues (ERP023317). Cluster-specific genes in scRNA-seq profiling were identified by Wilcoxon rank sum test using FindAllMarkers in Seurat with min.pct = 0.25 and adjusted P value < 0.05. Bulk RNA-seq profiling contained five time points, with three pools of retinal organoids at each time point. scRNA-seq profiling contained 1,130 single cells dissociated from 10 248-d retinal organoids. Single-nuclei RNA-seq profiling contained 1,375 single cells dissociated from 4-mm macular punch.

Electrophysiology and Imaging. Electrophysiological recording and two-photon imaging were performed as previously described (71–73). See *SI Appendix, Supplemental Materials and Methods* for details.

ACKNOWLEDGMENTS. We thank Drs. R. Chuck for support, Peng Wu for expert advice in multiphoton microscopy, and J. Nathans for antibodies; M.R.G. Stem Cell Institute (supported by New York State Stem Cell Science Grant C029154); and the Analytical Imaging Facility at Albert Einstein College of Medicine (AECOM) for service (supported by Grant P30CA013330). This work was supported by BrightFocus Grant M2012044 (to W.L.); Retina Research Foundation (R.C.); National Eye Institue Grants R01EY022645 (to W.L.), R01EY012200, and R01EY014237 (to A.C.), EY014800 (to M.M.D.), R01EY018571 and R01EY022356 (to R.C.), and R01EY026065 and R01EY17353 (to Z.J.Z.); unrestricted grants from Research to Prevent Blindness to the Department of Ophthalmology and Visual Sciences at AECOM and the Department of Ophthalmology & Visual Sciences at The University of Utah; the Carl Marshal & Mildred Almen Reeves Foundation (M.M.D.); Macular Degeneration Foundation (M.M.D.); National Institute of General Medical Sciences Grant T32GM007491 (to A.L.); Marvin L. Sears Professorship (Z.J.Z.); and Yale Vision Science Core (supported by Grant P30EY026878). Bulk and single-cell RNA-Seq were performed at the Single Cell Genomics Core at Baylor College of Medicine partially supported by NIH shared instrument Grants S10OD018033 and S10OD023469 and P30EY002520 (to R.C.). Support for The Einstein Training Program in Stem Cell Research of Albert Einstein College of Medicine, Inc. is acknowledged from the Empire State Stem Cell Fund through New York State Department of Health Contract C30292GG.

1. Veleri S, et al. (2015) Biology and therapy of inherited retinal degenerative disease: Insights from mouse models. *Dis Model Mech* 8:109–129.
2. Lancaster MA, Knoblich JA (2014) Organogenesis in a dish: Modeling development and disease using organoid technologies. *Science* 345:1247125.
3. Stern JH, et al. (2018) Regenerating eye tissues to preserve and restore vision. *Cell Stem Cell* 22:834–849.
4. Eiraku M, et al. (2011) Self-organizing optic-cup morphogenesis in three-dimensional culture. *Nature* 472:51–56.
5. Meyer JS, et al. (2011) Optic vesicle-like structures derived from human pluripotent stem cells facilitate a customized approach to retinal disease treatment. *Stem Cells* 29:1206–1218.
6. Nakano T, et al. (2012) Self-formation of optic cups and storable stratified neural retina from human ESCs. *Cell Stem Cell* 10:771–785.
7. Lowe A, Harris R, Bhansali P, Cvekl A, Liu W (2016) Intercellular adhesion-dependent cell survival and ROCK-regulated actomyosin-driven forces mediate self-formation of a retinal organoid. *Stem Cell Reports* 6:743–756.
8. Zhong X, et al. (2014) Generation of three-dimensional retinal tissue with functional photoreceptors from human iPSCs. *Nat Commun* 5:4047.
9. Reichman S, et al. (2014) From confluent human iPS cells to self-forming neural retina and retinal pigmented epithelium. *Proc Natl Acad Sci USA* 111:8518–8523.
10. Hiler D, et al. (2015) Quantification of retinogenesis in 3D cultures reveals epigenetic memory and higher efficiency in iPSCs derived from rod photoreceptors. *Cell Stem Cell* 17:101–115.
11. Wahlin KJ, et al. (2017) Photoreceptor outer segment-like structures in long-term 3D retinas from human pluripotent stem cells. *Sci Rep* 7:766.
12. Kaewkhaw R, et al. (2015) Transcriptome dynamics of developing photoreceptors in three-dimensional retina cultures recapitulates temporal sequence of human cone and rod differentiation revealing cell surface markers and gene networks. *Stem Cells* 33:3504–3518.
13. Li G, et al. (2018) Generation of retinal organoids with mature rods and cones from urine-derived human induced pluripotent stem cells. *Stem Cells Int* 2018:4968658.
14. Capowski EE, et al. (2018) Reproducibility and staging of 3D human retinal organoids across multiple pluripotent stem cell lines. *Development* 146:dev171686.
15. Parfitt DA, et al. (2016) Identification and correction of mechanisms underlying inherited blindness in human iPSC-derived optic cups. *Cell Stem Cell* 18:769–781.
16. Eldred KC, et al. (2018) Thyroid hormone signaling specifies cone subtypes in human retinal organoids. *Science* 362:eaau6348.
17. Hallam D, et al. (2018) Human-induced pluripotent stem cells generate light responsive retinal organoids with variable and nutrient-dependent efficiency. *Stem Cells* 36:1535–1551.
18. Phillips MJ, et al. (2018) A novel approach to single cell RNA-sequence analysis facilitates in silico gene reporting of human pluripotent stem cell-derived retinal cell types. *Stem Cells* 36:313–324.
19. Collin J, et al. (December 12, 2018) Deconstructing retinal organoids: Single cell RNA-seq reveals the cellular components of human pluripotent stem cell-derived retina. *Stem Cells*, 10.1002/stem.2963.
20. Macosko EZ, et al. (2015) Highly parallel genome-wide expression profiling of individual cells using nanoliter droplets. *Cell* 161:1202–1214.
21. Siegert S, et al. (2012) Transcriptional code and disease map for adult retinal cell types. *Nat Neurosci* 15:487–495.
22. Aldiri I, et al. (2017) The dynamic epigenetic landscape of the retina during development, reprogramming, and tumorigenesis. *Neuron* 94:550–568.e10.
23. Hoshino A, et al. (2017) Molecular anatomy of the developing human retina. *Dev Cell* 43:763–779.e4.
24. Welby E, et al. (2017) Isolation and comparative transcriptome analysis of human fetal and iPSC-derived cone photoreceptor cells. *Stem Cell Reports* 9:1898–1915.
25. Farkas MH, et al. (2013) Transcriptome analyses of the human retina identify unprecedented transcript diversity and 3.5 Mb of novel transcribed sequence via significant alternative splicing and novel genes. *BMC Genomics* 14:486.
26. Pinelli M, et al. (2016) An atlas of gene expression and gene co-regulation in the human retina. *Nucleic Acids Res* 44:5773–5784.
27. Li M, et al. (2014) Comprehensive analysis of gene expression in human retina and supporting tissues. *Hum Mol Genet* 23:4001–4014.
28. Peng YR, et al. (2019) Molecular classification and comparative taxonomics of foveal and peripheral cells in primate retina. *Cell* 176:1222–1237.e22.
29. Liu W, Lagutin O, Swindell E, Jamrich M, Oliver G (2010) Neuroretina specification in mouse embryos requires Six3-mediated suppression of Wnt8b in the anterior neural plate. *J Clin Invest* 120:3568–3577.
30. Gan L, et al. (1996) POU domain factor Brn-3b is required for the development of a large set of retinal ganglion cells. *Proc Natl Acad Sci USA* 93:3920–3925.
31. Sato S, et al. (2007) Dkk3-Cre BAC transgenic mouse line: A tool for highly efficient gene deletion in retinal progenitor cells. *Genesis* 45:502–507.
32. Hendrickson A, Possin D, Vajzovic L, Toth CA (2012) Histologic development of the human fovea from midgestation to maturity. *Am J Ophthalmol* 154:767–778.e2.
33. Curcio CA, Sloan KR, Kalina RE, Hendrickson AE (1990) Human photoreceptor topography. *J Comp Neurol* 292:497–523.
34. Lowe A, Dharmat R, Li Y, Chen R, Liu W (2019) Generation, transcriptome profiling, and functional validation of single cells from cone-enriched human retinal organoids. Gene Expression Omnibus. Available at https://www.ncbi.nlm.nih.gov/geo/query/acc.cgi?acc=GSE119274. Deposited August 30, 2018.
35. Simon R, et al. (2007) Analysis of gene expression data using BRB-ArrayTools. *Cancer Inform* 3:11–17.
36. Huang DW, et al. (2007) The DAVID gene functional classification tool: A novel biological module-centric algorithm to functionally analyze large gene lists. *Genome Biol* 8:R183.
37. Cepko C (2014) Intrinsically different retinal progenitor cells produce specific types of progeny. *Nat Rev Neurosci* 15:615–627.
38. Swaroop A, Kim D, Forrest D (2010) Transcriptional regulation of photoreceptor development and homeostasis in the mammalian retina. *Nat Rev Neurosci* 11:563–576.
39. Yeo G, Holste D, Kreiman G, Burge CB (2004) Variation in alternative splicing across human tissues. *Genome Biol* 5:R74.
40. Merkin J, Russell C, Chen P, Burge CB (2012) Evolutionary dynamics of gene and isoform regulation in Mammalian tissues. *Science* 338:1593–1599.
41. Zelinger L, Swaroop A (2018) RNA biology in retinal development and disease. *Trends Genet* 34:341–351.
42. Hao H, et al. (2014) Regulation of a novel isoform of receptor expression enhancing protein REEP6 in rod photoreceptors by bZIP transcription factor NRL. *Hum Mol Genet* 23:4260–4271.
43. Arno G, et al.; UKIRDC (2016) Mutations in REEP6 cause autosomal-recessive retinitis pigmentosa. *Am J Hum Genet* 99:1305–1315.
44. Agrawal SA, et al. (2017) REEP6 deficiency leads to retinal degeneration through disruption of ER homeostasis and protein trafficking. *Hum Mol Genet* 26:2667–2677.
45. Lowe A, Dharmat R, Li Y, Chen R, Liu W (2019) Generation, transcriptome profiling, and functional validation of single cells from cone-enriched human retinal organoids. Gene Expression Omnibus. https://www.ncbi.nlm.nih.gov/geo/query/acc.cgi?acc=GSE119343. Deposited August 31, 2018.
46. Liang Q, et al. (2019) Single-nuclei RNA-seq on human retinal tissue provides improved transcriptome profiling. bioRxiv:468207. Preprint, posted November 11, 2018.
47. Owen LA, et al. (2019) The Utah protocol for postmortem eye phenotyping and molecular biochemical analysis. *Invest Ophthalmol Vis Sci* 60:1204–1212.
48. Grindberg RV, et al. (2013) RNA-sequencing from single nuclei. *Proc Natl Acad Sci USA* 110:19802–19807.
49. Barrow AJ, Wu SM (2009) Low-conductance HCN1 ion channels augment the frequency response of rod and cone photoreceptors. *J Neurosci* 29:5841–5853.
50. Barnes S, Hille B (1989) Ionic channels of the inner segment of tiger salamander cone photoreceptors. *J Gen Physiol* 94:719–743.
51. Maricq AV, Korenbrot JI (1990) Inward rectification in the inner segment of single retinal cone photoreceptors. *J Neurophysiol* 64:1917–1928.
52. Altomare C, et al. (2001) Integrated allosteric model of voltage gating of HCN channels. *J Gen Physiol* 117:519–532.
53. Stieber J, Stöckl G, Herrmann S, Hassfurth B, Hofmann F (2005) Functional expression of the human HCN3 channel. *J Biol Chem* 280:34635–34643.
54. Moosmang S, et al. (2001) Cellular expression and functional characterization of four hyperpolarization-activated pacemaker channels in cardiac and neuronal tissues. *Eur J Biochem* 268:1646–1652.
55. Kawai F, et al. (2005) Suppression by an h current of spontaneous Na+ action potentials in human cone and rod photoreceptors. *Invest Ophthalmol Vis Sci* 46:390–397.
56. Sharon D, Blackshaw S, Cepko CL, Dryja TP (2002) Profile of the genes expressed in the human peripheral retina, macula, and retinal pigment epithelium determined through serial analysis of gene expression (SAGE). *Proc Natl Acad Sci USA* 99:315–320.
57. Brzezinski JA, Reh TA (2015) Photoreceptor cell fate specification in vertebrates. *Development* 142:3263–3273.
58. Roberts MR, Srinivas M, Forrest D, Morreale de Escobar G, Reh TA (2006) Making the gradient: Thyroid hormone regulates cone opsin expression in the developing mouse retina. *Proc Natl Acad Sci USA* 103:6218–6223.
59. Kelley MW, Turner JK, Reh TA (1994) Retinoic acid promotes differentiation of photoreceptors in vitro. *Development* 120:2091–2102.
60. Obata S, Usukura J (1992) Morphogenesis of the photoreceptor outer segment during postnatal development in the mouse (BALB/c) retina. *Cell Tissue Res* 269:39–48.
61. Goldstein LD, et al. (2017) Massively parallel nanowell-based single-cell gene expression profiling. *BMC Genomics* 18:519.
62. Kim D, et al. (2013) TopHat2: Accurate alignment of transcriptomes in the presence of insertions, deletions and gene fusions. *Genome Biol* 14:R36.
63. Trapnell C, et al. (2010) Transcript assembly and quantification by RNA-seq reveals unannotated transcripts and isoform switching during cell differentiation. *Nat Biotechnol* 28:511–515.
64. Love MI, Huber W, Anders S (2014) Moderated estimation of fold change and dispersion for RNA-seq data with DESeq2. *Genome Biol* 15:550.
65. de Hoon MJ, Imoto S, Nolan J, Miyano S (2004) Open source clustering software. *Bioinformatics* 20:1453–1454.
66. Kim D, Langmead B, Salzberg SL (2015) HISAT: A fast spliced aligner with low memory requirements. *Nat Methods* 12:357–360.
67. Pertea M, Kim D, Pertea GM, Leek JT, Salzberg SL (2016) Transcript-level expression analysis of RNA-seq experiments with HISAT, StringTie and Ballgown. *Nat Protoc* 11:1650–1667.
68. Katz Y, Wang ET, Airoldi EM, Burge CB (2010) Analysis and design of RNA sequencing experiments for identifying isoform regulation. *Nat Methods* 7:1009–1015.
69. Shekhar K, et al. (2016) Comprehensive classification of retinal bipolar neurons by single-cell transcriptomics. *Cell* 166:1308–1323.e30.
70. Johnson WE, Li C, Rabinovic A (2007) Adjusting batch effects in microarray expression data using empirical Bayes methods. *Biostatistics* 8:118–127.
71. Zhou ZJ (1998) Direct participation of starburst amacrine cells in spontaneous rhythmic activities in the developing mammalian retina. *J Neurosci* 18:4155–4165.
72. Zheng JJ, Lee S, Zhou ZJ (2004) A developmental switch in the excitability and function of the starburst network in the mammalian retina. *Neuron* 44:851–864.
73. Lee S, Zhang Y, Chen M, Zhou ZJ (2016) Segregated glycine-glutamate co-transmission from vGluT3 amacrine cells to contrast-suppressed and contrast-enhanced retinal circuits. *Neuron* 90:27–34.
74. Kent WJ, et al. (2002) The human genome browser at UCSC. *Genome Res* 12:996–1006.